

See discussions, stats, and author profiles for this publication at: <https://www.researchgate.net/publication/235791076>

# Lithium Insertion into Niobates with Columbite-Type Structure: Interplay between Structure-Composition and Crystallite Size

ARTICLE *in* THE JOURNAL OF PHYSICAL CHEMISTRY C · DECEMBER 2011

Impact Factor: 4.77 · DOI: 10.1021/jp206505y

---

CITATIONS

7

---

READS

31

## 2 AUTHORS:



**Anji Reddy Munnangi**

Helmholtz-Institut Ulm

35 PUBLICATIONS 393 CITATIONS

SEE PROFILE



**U. V. Varadaraju**

Indian Institute of Technology Madras

101 PUBLICATIONS 974 CITATIONS

SEE PROFILE

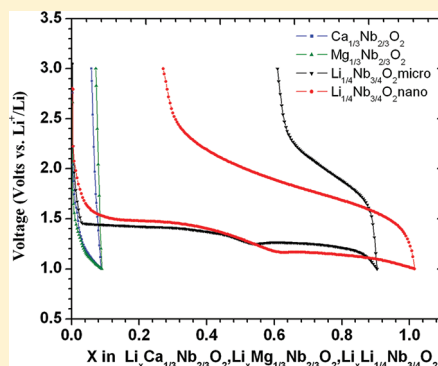
# Lithium Insertion into Niobates with Columbite-Type Structure: Interplay between Structure-Composition and Crystallite Size

M. Anji Reddy and U. V. Varadaraju\*

Materials Science Research Centre and Department of Chemistry, Indian Institute of Technology Madras, Chennai 600036, India

Supporting Information

**ABSTRACT:** We have studied lithium insertion into three columbite type compounds  $\text{MgNb}_2\text{O}_6$ ,  $\text{CaNb}_2\text{O}_6$ , and  $\text{LiNb}_3\text{O}_8$ . In the case of  $\text{MgNb}_2\text{O}_6$  and  $\text{CaNb}_2\text{O}_6$  only 0.27 and 0.26 Li are inserted, respectively. However, in the case of isostructural  $\text{LiNb}_3\text{O}_8$ , 3.6 Li are inserted. The large uptake of lithium in the case of  $\text{LiNb}_3\text{O}_8$  compared to those of  $\text{MgNb}_2\text{O}_6$  and  $\text{CaNb}_2\text{O}_6$  is discussed with regard to the presence of framework lithium and its distribution in  $\text{LiNb}_3\text{O}_8$ . Ex situ XRD studies reveal that the structure is stable up to the insertion of  $2.0\text{Li}/\text{LiNb}_3\text{O}_8$ . Further insertion of lithium leads to irreversible structural transformation. The initial discharge capacity of micrometer sized  $\text{LiNb}_3\text{O}_8$  is  $234\text{ mAh g}^{-1}$ . However it shows a large irreversible capacity loss in the first charge and the reversible capacity fades to  $45\text{ mAh g}^{-1}$  on cycling. Further, we have synthesized nanocrystalline  $\text{LiNb}_3\text{O}_8$  by polymeric complex method with the aim to improve its electrochemical performance. The nanocrystalline sample shows an initial discharge capacity of  $265\text{ mAh g}^{-1}$  and the reversible capacity is  $145\text{ mAh g}^{-1}$  even after 50 cycles, rendering nanocrystalline  $\text{LiNb}_3\text{O}_8$  as an attractive anode material for Li-ion batteries.



## INTRODUCTION

Lithium insertion into titanium and niobium based oxides has gained continuing attention for its potential in anode materials compared to carbon based materials, in terms of safety and reliability. In this context, various titanium and niobium oxides with different structural types have been explored.<sup>1–14</sup> Martinez-de la Cruz et al. investigated on electrochemical lithium insertion into  $\text{MNb}_2\text{O}_6$  ( $M = \text{Mn, Co, Ni, Cu, Zn, and Cd}$ ) with columbite type structure.<sup>15</sup> Their results showed that only a very small amount of lithium can be inserted into these compounds above 1.0 V. Kumuda and Kinomura reported that  $\text{CuNb}_2\text{O}_6$  exhibited reaction with 2.5 Li, and it is due to the extrusion of copper from the lattice.<sup>16</sup> Despite the fact that the structure is amenable for Li insertion, these compounds are hitherto shown to be less electro active. In the present study we have studied lithium insertion into three compounds  $\text{MgNb}_2\text{O}_6$ ,  $\text{CaNb}_2\text{O}_6$ , and  $\text{LiNb}_3\text{O}_8$  with columbite type structure. Herein we establish that the presence of framework lithium can facilitate the lithium insertion into columbite type of structures. Further, we emphasize the crystallite size effect on lithium insertion into  $\text{LiNb}_3\text{O}_8$ .

$\text{MgNb}_2\text{O}_6$  and  $\text{CaNb}_2\text{O}_6$  crystallize in the orthorhombic space group  $Pbcn$  with lattice parameters  $a = 14.18\text{ \AA}$ ,  $b = 5.700\text{ \AA}$ , and  $c = 5.033\text{ \AA}$  and  $a = 14.92\text{ \AA}$ ,  $b = 5.752\text{ \AA}$ , and  $c = 5.204\text{ \AA}$ , respectively.<sup>17,18</sup> Figure 1a shows the crystal structure of  $(\text{Mg, Ca})\text{Nb}_2\text{O}_6$ . The structure is built-up of  $(\text{Mg, Ca})\text{O}_6$  and  $\text{NbO}_6$  octahedra sharing edges and forming zigzag chains along the  $c$  axis (Figure 1b), and these chains run parallel to the  $b$  axis.

These layers are stacked along the  $a$  axis with regular alternation of two layers of Nb and one layer of  $(\text{Ca, Mg})$ ; the layers are

connected to each other by corner sharing.  $\text{LiNb}_3\text{O}_8$  crystallizes in the monoclinic space group  $P21/a$  with lattice parameters  $a = 15.262\text{ \AA}$ ,  $b = 5.033\text{ \AA}$ ,  $c = 7.457\text{ \AA}$ , and  $\beta = 107.34^\circ$ .<sup>19</sup> Figure 1c shows the crystal structure of  $\text{LiNb}_3\text{O}_8$ . The structure is built-up of  $\text{NbO}_6$  and  $\text{Nb/LiO}_6$  octahedra sharing edges and forming zigzag chains (Figure 1d) along the  $b$  axis and these chains run parallel to the  $b$  axis to form layers. These layers run parallel to the  $c$  axis with regular alternation of  $\text{NbO}_6$  edge sharing chains and  $\text{Nb/LiO}_6$  edge sharing chains. These identical layers are stacked along the  $a$  axis and each layer is connected to other layer by corner sharing. Such an structural arrangement leads to the formation of  $1 \times 1$  zigzag channels where lithium can be inserted.

## EXPERIMENTAL SECTION

Micrometer-sized samples of  $\text{MgNb}_2\text{O}_6$ ,  $\text{CaNb}_2\text{O}_6$ , and  $\text{LiNb}_3\text{O}_8$  were prepared by conventional solid state reaction (SSR) in air. The starting reagents are  $\text{Mg}(\text{CH}_3\text{COO})_2 \cdot 4\text{H}_2\text{O}$  (Fulka, 99%),  $\text{CaCO}_3$  (Merck, 99.5%),  $\text{Li}_2\text{CO}_3$  (Merck, 99%), and  $\text{Nb}_2\text{O}_5$  (Alfa, 99.9%). Stoichiometric amounts of reactants were ground and calcined at 400, 800, and 600 °C for  $\text{MgNb}_2\text{O}_6$ ,  $\text{CaNb}_2\text{O}_6$ , and  $\text{LiNb}_3\text{O}_8$  respectively. The resultant powders were ground well and finally calcined at 1200 °C for 24 h. In the case of  $\text{LiNb}_3\text{O}_8$ , 5 wt %  $\text{Li}_2\text{CO}_3$  was taken in excess in order to compensate for the  $\text{Li}_2\text{O}$  loss at higher temperatures. Nanocrystalline  $\text{LiNb}_3\text{O}_8$  was prepared by the polymerizable complex (PC) method.

Received: July 9, 2011

Revised: October 8, 2011

Published: November 04, 2011

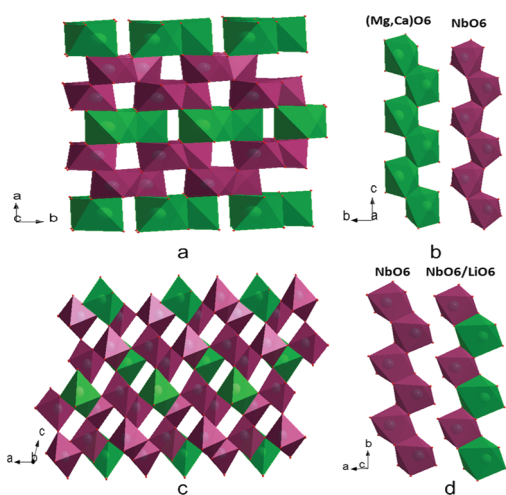


**Figure 1.** (a) Crystal structure of (Mg, Ca)Nb<sub>2</sub>O<sub>6</sub> along <001> or in the *ab* plane; (b) (Mg, Ca)O<sub>6</sub> and NbO<sub>6</sub> edge shared octahedra along *c*; (c) Crystal structure of LiNb<sub>3</sub>O<sub>8</sub> in *ac* plane or along <010>; (d) Nb/LiO<sub>6</sub> and NbO<sub>6</sub> edge shared octahedra along *b*.

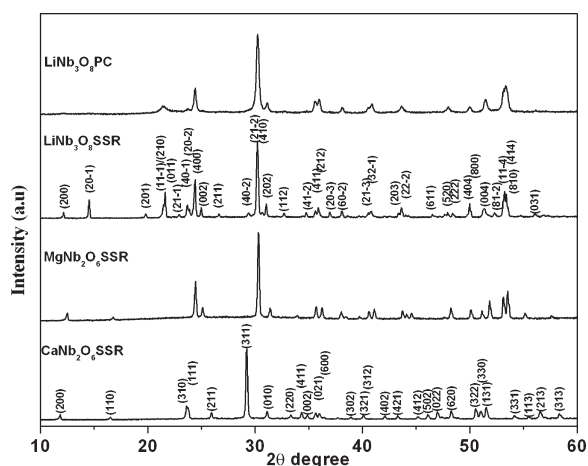


**Figure 2.** PXRD patterns of CaNb<sub>2</sub>O<sub>6</sub>, MgNb<sub>2</sub>O<sub>6</sub>, and LiNb<sub>3</sub>O<sub>8</sub> synthesized by SSR and polymeric complex (PC) method.

The starting precursors used for this method were Nb<sub>2</sub>O<sub>5</sub>·*x*H<sub>2</sub>O and Li<sub>2</sub>CO<sub>3</sub>. Nb<sub>2</sub>O<sub>5</sub>·*x*H<sub>2</sub>O was prepared according to the reported procedure.<sup>14</sup> In the present case, the value of *x* was estimated to be 4.25 from thermo gravimetric analysis. In the first step, a requisite amount of citric acid (CA; Spectrochem, 99.7%) was dissolved in distilled water, and the resulting solution was kept at 60 °C. Nb<sub>2</sub>O<sub>5</sub>·*x*H<sub>2</sub>O was dissolved in this solution. After complete dissolution of Nb<sub>2</sub>O<sub>5</sub>·*x*H<sub>2</sub>O, Li<sub>2</sub>CO<sub>3</sub> was added and the solution was maintained at 60 °C for a few hours in order to ensure the metal-complex formation. Ethylene glycol (EG) was added, and the temperature was raised to 90 °C to facilitate the polyesterification step. The metal/CA/EG ratio was maintained as 1:4:16. The obtained gel was dried at 120 °C and decomposed by heating in air at 300 °C for 4 h. The resulting powder was calcined at 600 °C for 2 h to obtain nanocrystalline LiNb<sub>3</sub>O<sub>8</sub>.

The phase purity of the synthesized samples was checked using Rigaku mini flex XRD (Japan) using Cu K $\alpha$  radiation. A scanning electron microscope (SEM) Philips Field Effect Gun (FEG) XL-30

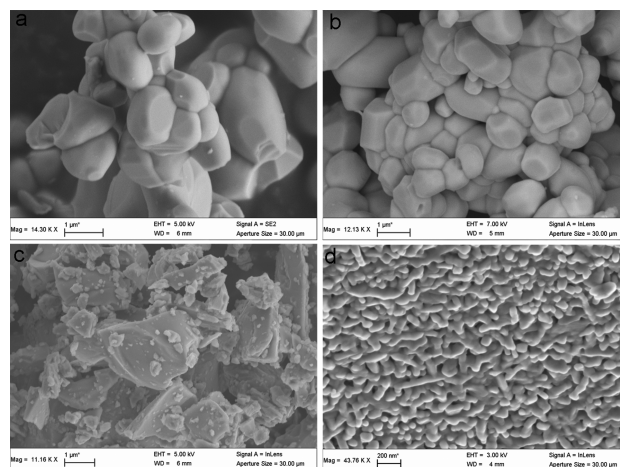


**Figure 3.** SEM images of (a) CaNb<sub>2</sub>O<sub>6</sub>, (b) MgNb<sub>2</sub>O<sub>6</sub>, and (c) LiNb<sub>3</sub>O<sub>8</sub> synthesized by SSR and (d) LiNb<sub>3</sub>O<sub>8</sub> synthesized by PC method.

is used to study the morphology of the samples. Electrodes were fabricated by mixing active material, acetylene black (Denka Singapore Pvt. Ltd.) and poly(vinylidene fluoride) (PVDF) in the weight ratios 70:20:10. Slurry containing the above mixture was prepared by using *N*-methyl-2-pyrrolidinone and was spread on a stainless steel foil and dried in an oven at 100 °C for 12 h. Swagelok cells were used for electrochemical studies. The cells were fabricated in an argon filled glovebox (mBraun, Germany) with Li foil as the anode, Teklon (Entek, U.S.A.) as a separator, and 1 M LiPF<sub>6</sub> in 1:1 ethylene carbonate plus dimethyl carbonate as the electrolyte (Chiel Industries Ltd., Korea). Charge discharge cycling of the cells was carried out in galvanostatic mode at RT by using Arbin battery cycling unit (BT2000, U.S.A.). Ex situ XRD patterns were collected on electrodes discharged and charged to various stages. The electrodes were covered with Mylar film and XRD patterns were obtained.

## RESULTS AND DISCUSSION

Figure 2 shows the powder XRD patterns of CaNb<sub>2</sub>O<sub>6</sub>, MgNb<sub>2</sub>O<sub>6</sub>, and LiNb<sub>3</sub>O<sub>8</sub> synthesized by solid state reaction (SSR) and by polymeric complex (PC) method. Phase pure samples were obtained in the case of samples prepared by SSR. However, in the case of LiNb<sub>3</sub>O<sub>8</sub> prepared by PC method, a small amount of LiNbO<sub>3</sub> was found. Figure 3 shows the SEM images of MgNb<sub>2</sub>O<sub>6</sub>, CaNb<sub>2</sub>O<sub>6</sub>, and LiNb<sub>3</sub>O<sub>8</sub> SSR and LiNb<sub>3</sub>O<sub>8</sub> PC. In the case of samples prepared by SSR, the particle size is in the range of 0.5–5.0 μm. However, in the case of LiNb<sub>3</sub>O<sub>8</sub>, the particles are irregular in shape compared to those of (Mg/Ca)Nb<sub>2</sub>O<sub>6</sub>. Further, tiny particles are seen on the surface of the larger particles of LiNb<sub>3</sub>O<sub>8</sub>, which might arise due to the volatile nature of Li at higher temperatures. In the case of LiNb<sub>3</sub>O<sub>8</sub> synthesized by PC method, the particles are of nanometer size regime. The mean crystallite size calculated from Scherrer formula is 22.0 nm.

Figure 4a shows the voltage-composition profiles of MgNb<sub>2</sub>O<sub>6</sub>, CaNb<sub>2</sub>O<sub>6</sub>, and LiNb<sub>3</sub>O<sub>8</sub> synthesized by SSR. The discharge/charge curves are obtained at C/10 rate. When discharged at this rate, 0.27 Li in MgNb<sub>2</sub>O<sub>6</sub> and 0.26 Li in CaNb<sub>2</sub>O<sub>6</sub> are inserted, whereas in the case with LiNb<sub>3</sub>O<sub>8</sub>, 3.6 Li are inserted on discharge to 1.0 V, and on charge, 1.1 Li are extracted. On subsequent cycling 0.7 Li are

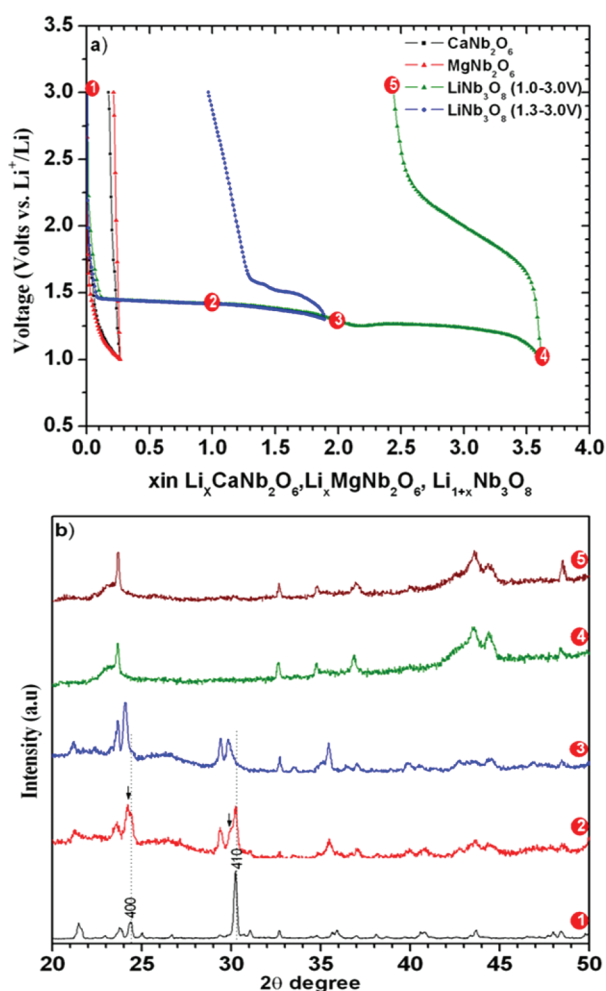


**Figure 4.** (a) Initial discharge–charge curves of micro-sized  $\text{MgNb}_2\text{O}_6$ ,  $\text{CaNb}_2\text{O}_6$ , and  $\text{LiNb}_3\text{O}_8$  obtained at C/10 rate. (b) Ex situ XRD patterns of micro-sized  $\text{LiNb}_3\text{O}_8$ ; the patterns are obtained at different insertion levels as shown in Figure 2a.

reversibly inserted. From the voltage-composition plot, it is evident that the insertion process occurs in three voltage regions. In the first region, 2.2–1.45 V, the voltage decreases smoothly with increasing Li content; 0.15 Li are inserted in this region. In the second region, 1.45–1.25 V, a plateau is observed at 1.4 V; 1.96 Li are inserted in this region. In the third region, 1.25–1.0 V, another plateau is observed at 1.24 V; 1.5 Li are inserted in this region. During charge, lithium is extracted over a wide voltage window with large polarization between discharge and charge processes. The large irreversible capacity loss (ICL) in the first cycle is attributed to the irreversible structural change. The discharge profile of second and subsequent cycles is similar but different from that of the first one (Figure S1(a), in the Supporting Information). This further suggests that, the structural changes occurred during the first discharge to 1.0 V are not reversible. The cutoff voltage is set to 1.3 V to arrest the plateau at 1.2 V and tested the cell behavior. In this case 1.9 Li are inserted and on charge 0.95 Li are extracted. On subsequent cycling, 1.0 Li is reversibly inserted (Figure S1(a), in the Supporting Information). Small polarization (0.1 V, from differential plot) is seen between the discharge and charge processes, when compared (0.7 V, from differential plot) to cycling between 3.0 and 1.0 V. The second discharge insertion potential is only slightly

different from the first discharge potential. This indicates that there are no irreversible structural changes at this stage. To study the structural changes during lithium insertion, ex situ XRD patterns were recorded on electrodes at various stages. Figure 4b shows the ex situ XRD patterns of micrometer-sized  $\text{LiNb}_3\text{O}_8$  recorded at various stages as marked in Figure 4a. After insertion of 1.0 Li, new peaks (shown with arrows in Figure 4b(2)) are seen adjacent to (400) and (410) peaks. During insertion of second lithium, these new peaks grown further at the expense of (400) and (410) (Figure 4b(3)). After the insertion of 3.6 Li (discharge to 1.0 V), the initial XRD pattern is completely changed (Figure 4b(4)). The XRD pattern of fully charged electrode (extraction of 1.1 Li) is similar to electrode discharged 1.0 V (Figure 4b(5)). On the basis of the voltage-composition behavior and ex situ XRD studies, the following mechanism is suggested. Initially, insertion of 0.15 Li forms solid solution with  $\text{LiNb}_3\text{O}_8$ . Further insertion leads to phase separation with composition  $\text{Li}_3\text{Nb}_3\text{O}_8$ , the structure of which is similar to that of the parent phase. Further insertion of lithium (>2.0 Li) leads to irreversible phase transformation.

The molecular formulas of the compounds  $\text{MgNb}_2\text{O}_6$ ,  $\text{CaNb}_2\text{O}_6$ , and  $\text{LiNb}_3\text{O}_8$  can be written as  $\text{Mg}_{1/3}\text{Nb}_{2/3}\text{O}_2$ ,  $\text{Ca}_{1/3}\text{Nb}_{2/3}\text{O}_2$ , and  $\text{Li}_{1/4}\text{Nb}_{3/4}\text{O}_2$ , respectively. The amount of Li that can be inserted in these compounds is 0.09 Li/ $\text{Mg}_{1/3}\text{Nb}_{2/3}\text{O}_2$ , 0.09 Li/ $\text{Ca}_{1/3}\text{Nb}_{2/3}\text{O}_2$ , and 0.9 Li/ $\text{Li}_{1/4}\text{Nb}_{3/4}\text{O}_2$ . Evidently  $\text{Li}_{1/3}\text{Nb}_{3/4}\text{O}_2$  shows higher electrochemical activity compared to  $\text{Mg}_{1/3}\text{Nb}_{2/3}\text{O}_2$  and  $\text{Ca}_{1/3}\text{Nb}_{2/3}\text{O}_2$ . To understand the factors influencing the lithium insertion in  $\text{MgNb}_2\text{O}_6$  and  $\text{CaNb}_2\text{O}_6$ , we have performed discharge–charge at a slow rate of C/50. At this slow rate, 0.5 Li and 0.9 Li are inserted in  $\text{MgNb}_2\text{O}_6$  and  $\text{CaNb}_2\text{O}_6$ , respectively (Figure S2, in the Supporting Information). However, upon charge no lithium is extracted. Even though both the samples show similar extent of lithium insertion at the C/10 rate (Figure 4a), a marked difference is seen in their activity at the C/50 rate. This can be rationalized based on the fact that the unit cell volume of  $\text{CaNb}_2\text{O}_6$  is  $111.69 \text{ \AA}^3$  and that of  $\text{MgNb}_2\text{O}_6$  is  $101.75 \text{ \AA}^3$ . This is due to the larger ionic radius of  $\text{Ca}^{2+}$  (1.0 Å) compared to that of  $\text{Mg}^{2+}$  (0.72 Å) in octahedral oxygen coordination. Further, the marked difference in the electroactivity at different C rates suggests that lithium insertion in these compounds is a diffusion controlled process. The origin for high electrochemical activity of  $\text{LiNb}_3\text{O}_8$  compared to (Mg,Ca) $\text{Nb}_2\text{O}_6$  is mainly attributed to the structure and composition of these compounds. The relatively small space available for lithium insertion, which can explain the low activity of  $\text{MgNb}_2\text{O}_6$  compared to that of  $\text{CaNb}_2\text{O}_6$  and one-dimensional nature of channels available for diffusion of lithium in the structure. Lithium being the diffusing ion (inserted species), the presence of  $\text{Li}^+$  in the framework of the structure rather than  $\text{M}^{2+}$  provides additional diffusion pathways for lithium in the structure. Further,  $\text{Li}^+$  present in each layer of  $\text{LiNb}_3\text{O}_8$  can facilitate the interlayer diffusion. Thus, the high Li insertion activity of  $\text{LiNb}_3\text{O}_8$  compared to isostructural  $\text{MNb}_2\text{O}_6$  (M = Mg and Ca) can be rationalized.

Although 3.6 Li/f.u is inserted into micrometer-sized  $\text{LiNb}_3\text{O}_8$  only 1.1 Li is extracted in the first charge and on subsequent charge only 0.7 Li are reversibly inserted, this corresponds to a reversible capacity of  $45 \text{ mAh g}^{-1}$ . Thus, in order to investigate the crystallite size effect on the reversible capacity we have studied the electrochemical properties of nanometer-sized  $\text{LiNb}_3\text{O}_8$ . Figure 5a shows the voltage-composition profiles of nanometer-sized  $\text{LiNb}_3\text{O}_8$  cycled in the voltage window 1.0–3.0 V. During the first discharge



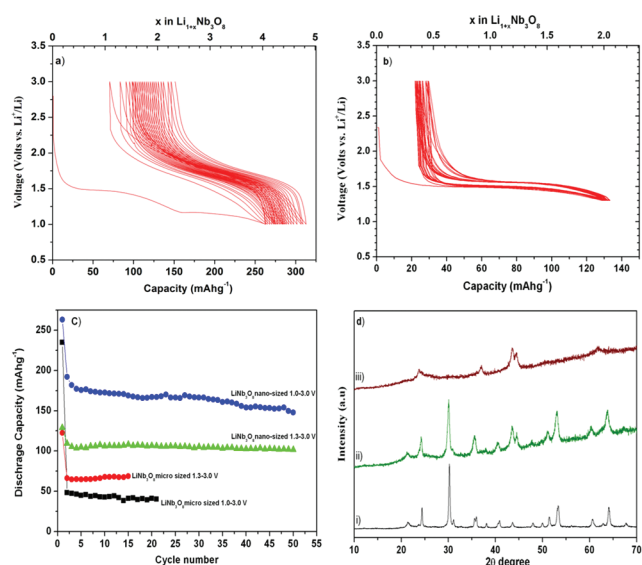


**Figure 5.** Voltage-composition profiles of nanosized  $\text{LiNb}_3\text{O}_8$  for the first 20 cycles, obtained at a C/10 rate in the voltage ranges (a) 1.0–3.0 and (b) 1.3–3.0 V. (c) Cycling behavior of micro-sized and nano-sized  $\text{LiNb}_3\text{O}_8$ , in the voltage windows 1.3–3.0 and 1.0–3.0 V. (d) XRD patterns of nanocrystalline  $\text{LiNb}_3\text{O}_8$  (i) pristine sample and (ii) after 50 cycles in the voltage window 1.3–3.0 V and (iii) after 50 cycles in the voltage range 1.0–3.0 V.

4.05  $\text{Li}/\text{LiNb}_3\text{O}_8$  are inserted, 0.45 Li more compare to micro-sized  $\text{LiNb}_3\text{O}_8$ . The first discharge capacity corresponds to  $265 \text{ mAh g}^{-1}$ . During first charge 3 Li are extracted, 1.9 Li more compare to micro-sized  $\text{LiNb}_3\text{O}_8$ . On subsequent cycling 2.6 Li are reversibly inserted. Figure 5b shows the voltage-composition profiles of nanometer-sized  $\text{LiNb}_3\text{O}_8$  in the voltage window 1.3–3.0 V. When the cutoff voltage is set to 1.3 V, 2.0 Li are inserted and on charge 1.63 Li are extracted. On subsequent cycling, 1.6 Li is reversibly inserted. It is important to note that, in this voltage window, the polarization between discharge and charge is much less and shows an excellent cycling stability. Figure 5d shows the ex-situ XRD patterns recorded on nano sized  $\text{LiNb}_3\text{O}_8$  after 50 cycles. The sample cycled between the 1.0–3.0 V (Figure 5d(iii)) shows completely new peaks suggesting the irreversible phase transformation. When cycled in the voltage range 1.3–3.0 V (Figure 5d(ii)), the initial phase peaks are present indicating the reversible structural changes during the initial insertion of 2.0 Li. However, few peaks correspond to the irreversible phase was seen and it could be due to the gradual transformation of phase as the cutoff voltage is 1.3 V, close to the phase transition voltage plateau. Figure 5c shows the cycling behavior of micrometer-sized and nanometer-sized  $\text{LiNb}_3\text{O}_8$  in different voltage ranges. The micrometer-sized sample show capacities of 70 and  $45 \text{ mAh g}^{-1}$ , when cycled in the voltage windows 1.3–3.0 and 1.0–3.0 V, respectively. The nanometer-sized sample shows reversible capacities of 145 and  $105 \text{ mAh g}^{-1}$  even after 50 cycles when cycled in the voltage windows 1.3–3.0 and 1.0–3.0 V, respectively. The high reversible capacity and cycling stability renders nanocrystalline  $\text{LiNb}_3\text{O}_8$  as an attractive anode material for lithium batteries. The higher reversible capacity of nanometer-sized  $\text{LiNb}_3\text{O}_8$  compared to micrometer-sized  $\text{LiNb}_3\text{O}_8$  is attributed to the reduced path lengths for lithium insertion and extraction. Further reduction of crystallite size and/or compositing with carbon can significantly enhance the reversible capacity of  $\text{LiNb}_3\text{O}_8$ .

## CONCLUSION

In conclusion, we demonstrated that the presence of framework lithium can facilitate the lithium insertion into columbite-type structures. Our results<sup>20</sup> on rutile  $\text{TiO}_2$  shows that such a concept can be implemented to similar structures as well. Further, we achieved a 3-fold enhancement in the reversible capacity of  $\text{LiNb}_3\text{O}_8$  by decreasing the crystallite size to nanometer range, demonstrating the crystallite size effect we emphasized upon.

## ASSOCIATED CONTENT

**S Supporting Information.** Charge discharge curves of  $(\text{Mg,Ca})\text{Nb}_2\text{O}_6$  at C/50 and charge discharge curves of micro-sized  $\text{LiNb}_3\text{O}_8$  for the first 10 cycles. This material is available free of charge via the Internet at <http://pubs.acs.org>.

## AUTHOR INFORMATION

### Corresponding Author

\*E-mail: [varada@iitm.ac.in](mailto:varada@iitm.ac.in).

## REFERENCES

- (1) Ferg, E.; Gummow, R. J.; De Kock, A.; Thackeray, M. M. *J. Electrochem. Soc.* **1994**, *141*, L147.
- (2) Ohzuku, T.; Ueda, A.; Yamamoto, N. *J. Electrochem. Soc.* **1995**, *142*, 1431.
- (3) Nakahara, K.; Nakajima, R.; Matsushima, T.; Majima, H. *J. Power Sources* **2003**, *117*, 131.
- (4) Marchand, R.; Brohan, L.; Tournoux, M. *Mater. Res. Bull.* **1980**, *15*, 1129.
- (5) Armstrong, A. R.; Armstrong, G.; Canales, J.; Garcia, R.; Bruce, P. G. *Adv. Mater.* **2005**, *17*, 862.
- (6) Huang, S. Y.; Kavan, L.; Exnar, I.; Gratzel, M. *J. Electrochem. Soc.* **1995**, *142*, L142.
- (7) Anji Reddy, M.; Satya Kishore, M.; Pralong, V.; Caignaert, V.; Varadaraju, U. V.; Raveau, B. *Electrochem. Commun.* **2006**, *8*, 1299.
- (8) Anji Reddy, M.; Satya Kishore, M.; Pralong, V.; Varadaraju, U. V.; Raveau, B. *Electrochem. Solid-State Lett.* **2007**, *10*, A29.
- (9) Reichman, H.; Bard, A. J. *J. Electrochem. Soc.* **1981**, *128*, 344.
- (10) Patoux, S.; Dolle, M.; Rousse, G.; Masquelier, C. *J. Electrochem. Soc.* **2002**, *149* (4), A391.
- (11) Kodama, R.; Terada, Y.; Nakai, I.; Komaba, S.; Kumagai, N. *J. Electrochem. Soc.* **2006**, *153* (3), A583.
- (12) Colin, J.-F.; Pralong, V.; Caignaert, V.; Hervieu, M.; Raveau, B. *Inorg. Chem.* **2006**, *45* (18), 7217.
- (13) Colin, J.-F.; Pralong, V.; Hervieu, M.; Caignaert, V.; Raveau, B. *Chem. Mater.* **2008**, *20* (4), 1534.
- (14) Anji Reddy, M.; Varadaraju, U. V. *Chem. Mater.* **2008**, *20* (14), 4557.
- (15) Martinez-de la Cruz, A.; Alcaraz, N. L.; Fuentes, A. F.; Torres-Martinez, L. M. *J. Power Sources* **1999**, *81–82*, 255.
- (16) Kumuda, N.; Kinomura, N. *Mater. Res. Bull.* **1990**, *25*, 881.
- (17) Cummings, J. P.; Simonsen, S. H. *Am. Mineral.* **1970**, *55* (1–2), 90.
- (18) Pagola, S.; Carbonio, R. E.; Alonso, J. A.; Fernández-Díaz, M. T. *J. Solid State Chem.* **1997**, *134*, 76.
- (19) Lundberg, M. *Acta Chem. Scand.* **1971**, *25* (9), 3337.
- (20) Reddy, M. A.; Varadaraju, U. V. manuscript in preparation.